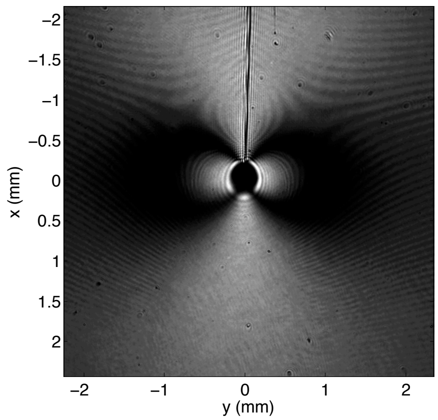

(a) $I_1 = I_o(1 + \cos(\delta))$

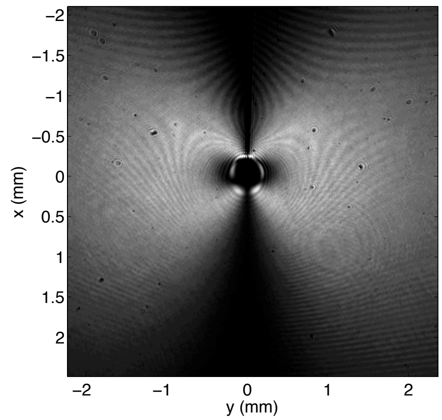

(b) $I_2 = I_o(1 - \cos(\delta))$

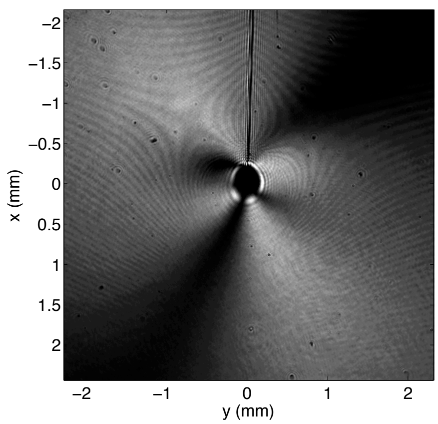

(c) $I_3 = I_o(1 - \sin(\delta)\sin(2\alpha))$

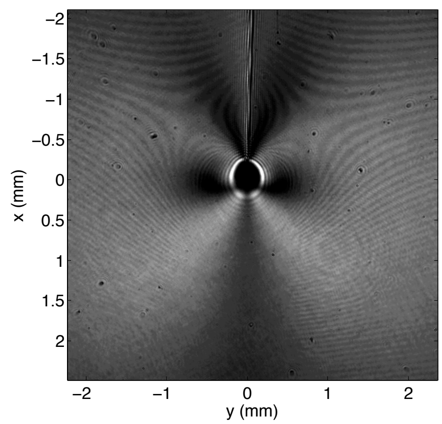

(d) $I_4 = I_o(1 + \sin(\delta)\cos(2\alpha))$

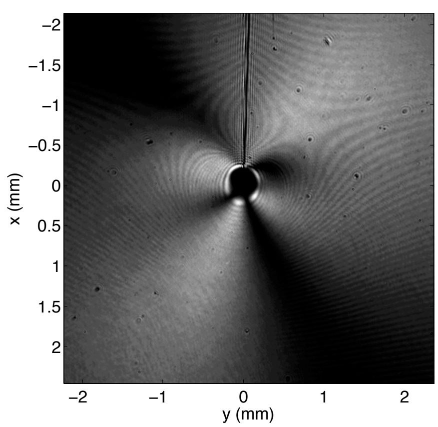

(e) $I_5 = I_o(1 + \sin(\delta)\sin(2\alpha))$

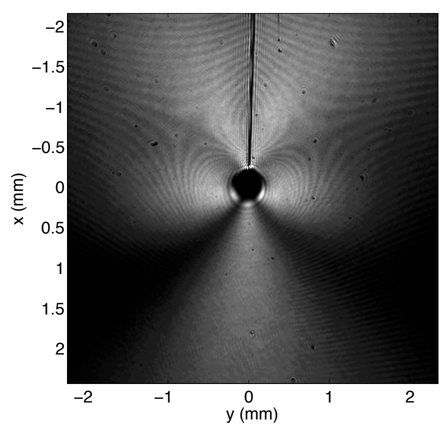

(f) $I_6 = I_o(1 - \sin(\delta)\cos(2\alpha))$

Figure 4.3: Experimental mages from six-step phase-shifting photoelasticity for specimen HomC1 for $K_I = 0.514$ MPa$\sqrt{\text{m}}$ and $K_{II} = 4.4$ kPa$\sqrt{\text{m}}$: Caustic shadows obscure the data at the crack tip due to the stress concentration, and the weak high density fringes overlaying the photoelastic fringes are due to the interference of the reflections from the front and back faces of the specimen.

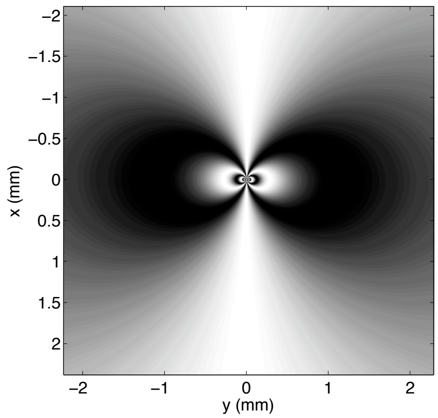

(a) $I_1 = I_o(1 + \cos(\delta))$

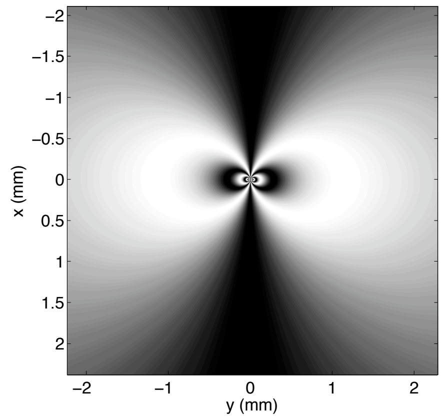

(b) $I_2 = I_o(1 - \cos(\delta))$

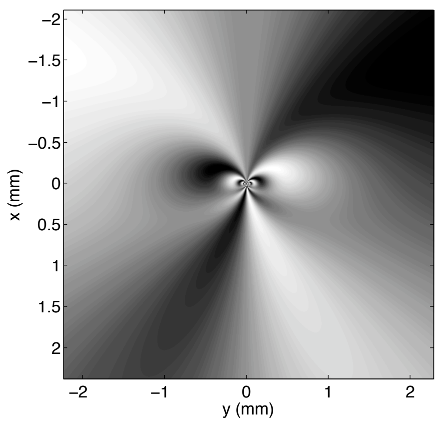

(c) $I_3 = I_o(1 - \sin(\delta)\sin(2\alpha))$

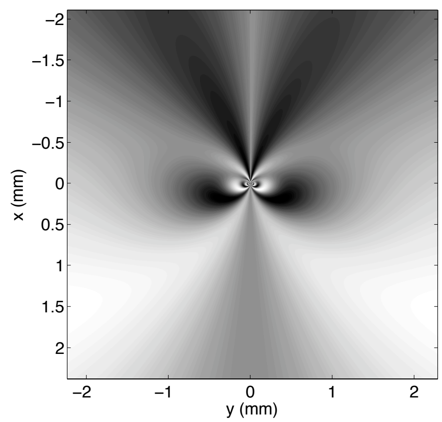

(d) $I_4 = I_o(1 + \sin(\delta)\cos(2\alpha))$

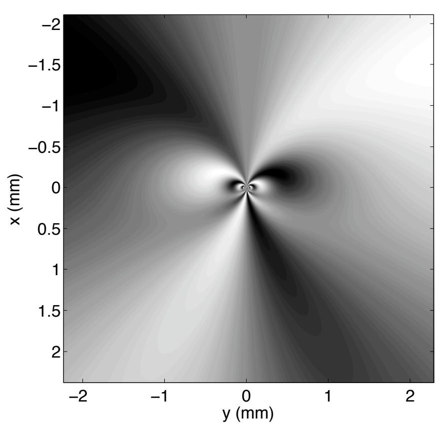

(e) $I_5 = I_o(1 + \sin(\delta)\sin(2\alpha))$

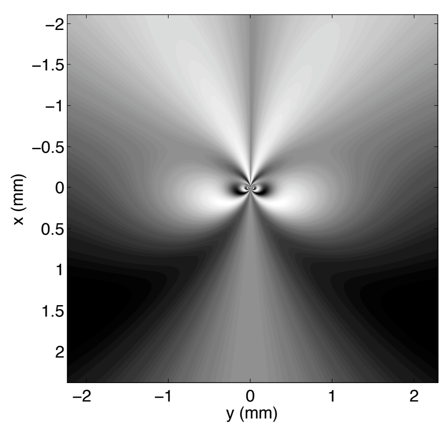

(f) $I_6 = I_o(1 - \sin(\delta)\cos(2\alpha))$

Figure 4.4: Theoretical mages from six-step phase-shifting photoelasticity for specimen HomC1 with $K_I = 0.514$ MPa$\sqrt{\text{m}}$ and $K_{II} = 4.4$ kPa$\sqrt{\text{m}}$, where I_o is uniform over the field of view, unlike the experimental images, where the intensity is Gaussian in nature

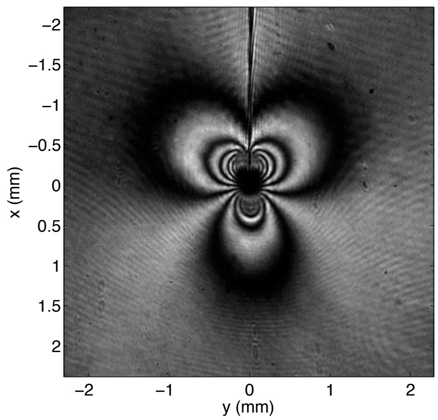

(a) I_1^{Ex}

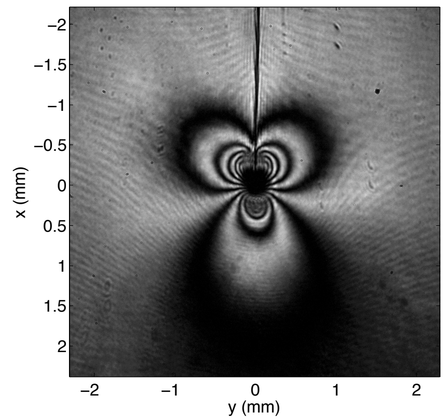

(b) I_2^{Ex}

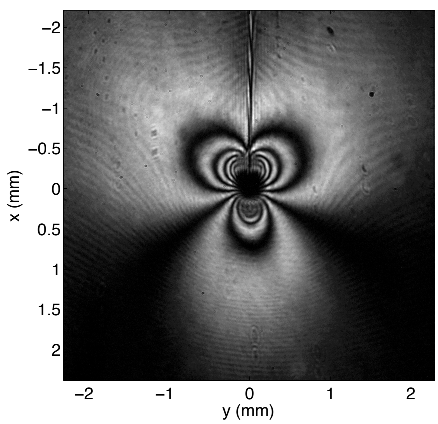

(c) I_3^{Ex}

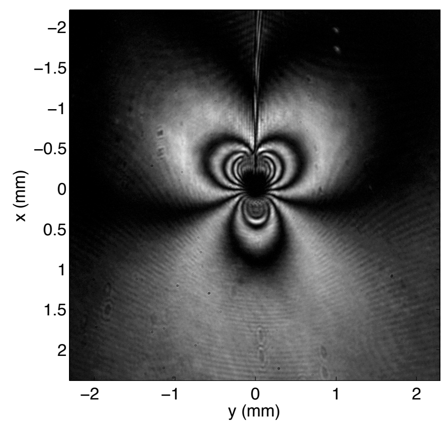

(d) I_4^{Ex}

Figure 4.5: Experimental phase-shifted images from vertical shearing CGS using pure $E_x\hat{\imath}$ input for specimen HomC1 for $K_I = 0.514$ MPa$\sqrt{\text{m}}$ and $K_{II} = 4.4$ kPa$\sqrt{\text{m}}$

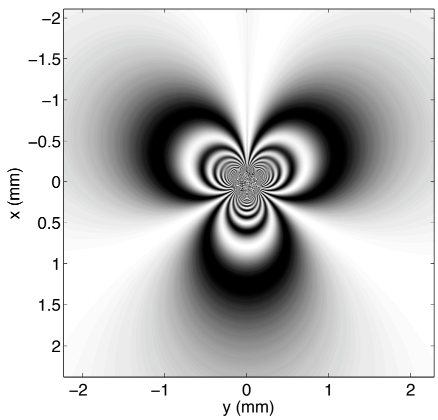

(a) I_1^{Ex}

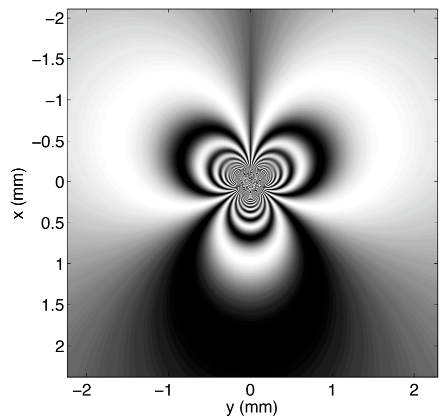

(b) I_2^{Ex}

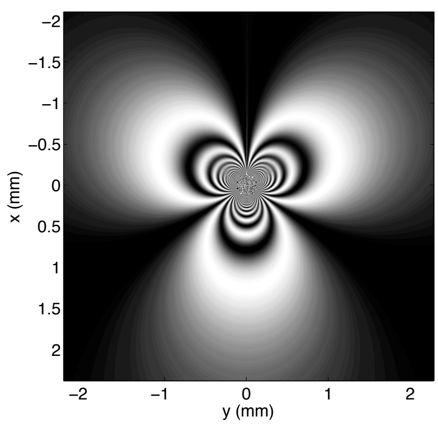

(c) I_3^{Ex}

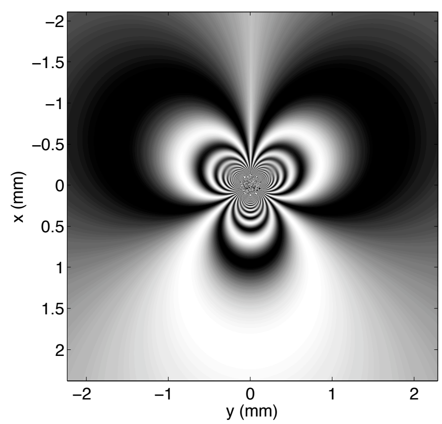

(d) I_4^{Ex}

Figure 4.6: Theoretical phase-shifted images from vertical shearing CGS using pure $E_x\hat{\imath}$ input for specimen HomC1 for $K_I = 0.514$ MPa$\sqrt{\text{m}}$ and $K_{II} = 4.4$ kPa$\sqrt{\text{m}}$

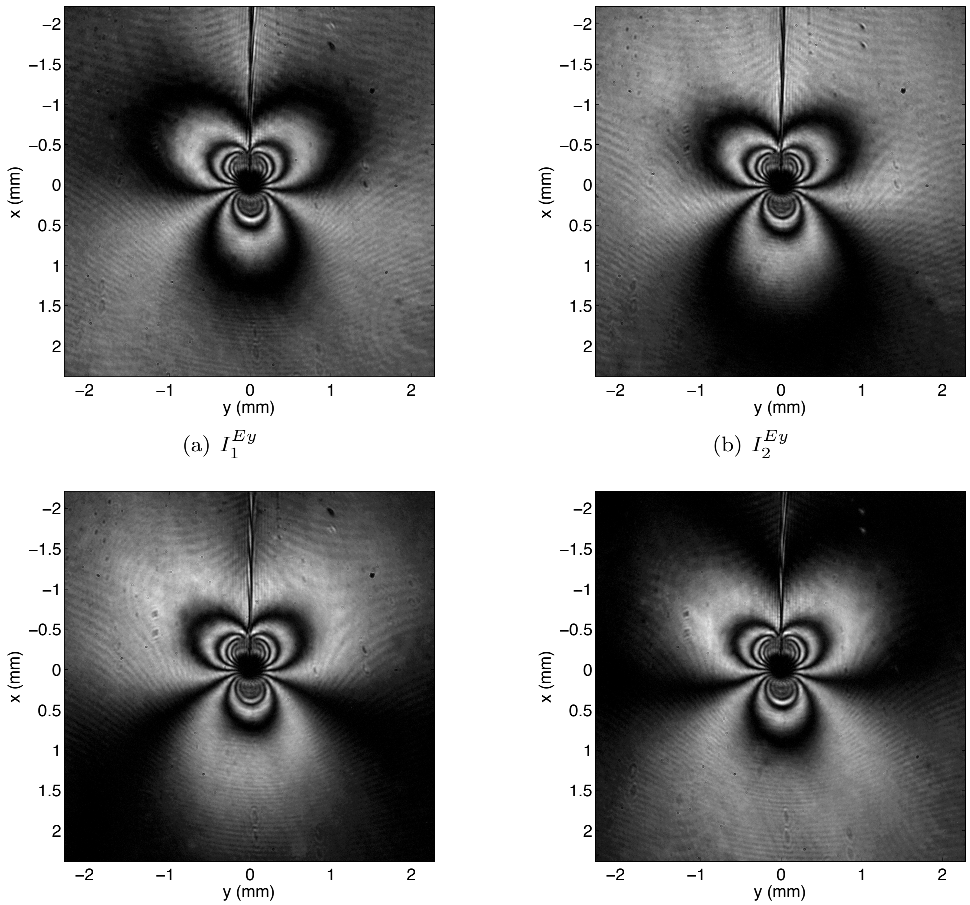

(a) I_1^{Ey}

(b) I_2^{Ey}

(c) I_3^{Ey}

(d) I_4^{Ey}

Figure 4.7: Experimental phase-shifted images from vertical shearing CGS using pure $E_y\hat{\jmath}$ input for specimen HomC1 for $K_I = 0.514\ \mathrm{MPa}\sqrt{\mathrm{m}}$ and $K_{II} = 4.4\ \mathrm{kPa}\sqrt{\mathrm{m}}$

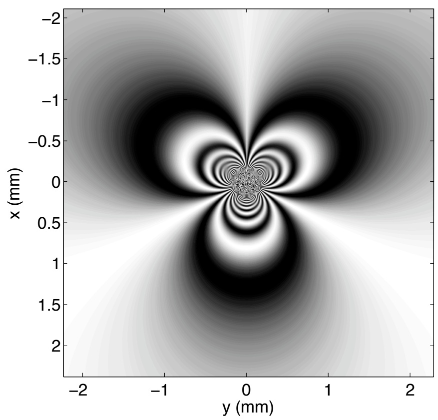

(a) I_1^{Ey}

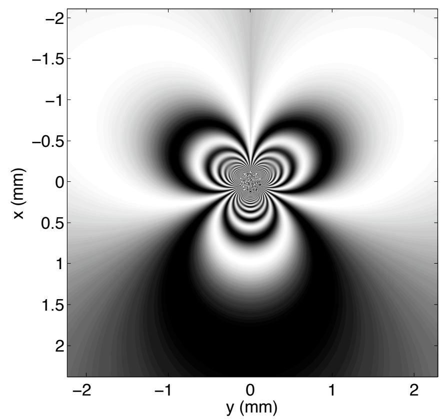

(b) I_2^{Ey}

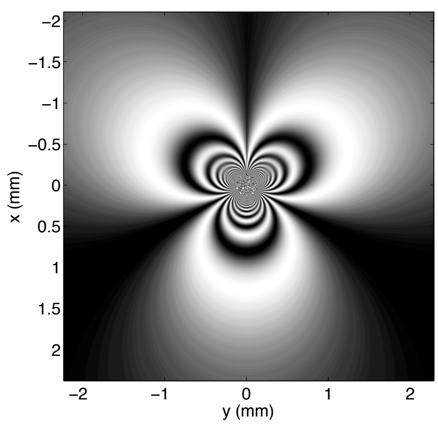

(c) I_3^{Ey}

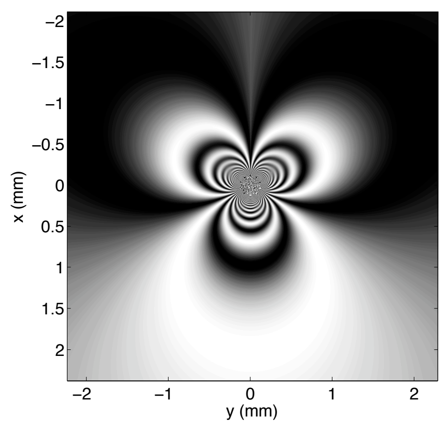

(d) I_4^{Ey}

Figure 4.8: Theoretical phase-shifted images from vertical shearing CGS using pure $E_y\hat{\jmath}$ input for specimen HomC1 for $K_I = 0.514$ MPa$\sqrt{\text{m}}$ and $K_{II} = 4.4$ kPa$\sqrt{\text{m}}$

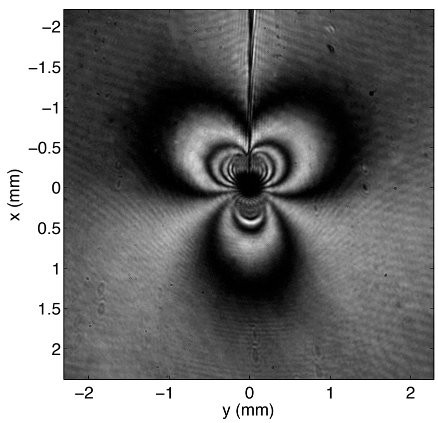

(a) I_1^{circ}

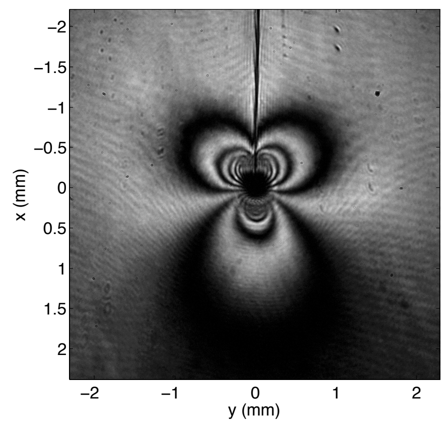

(b) I_2^{circ}

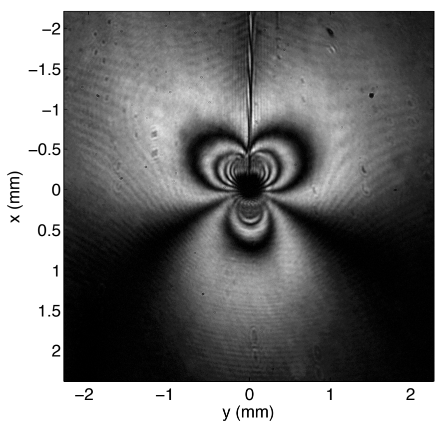

(c) I_3^{circ}

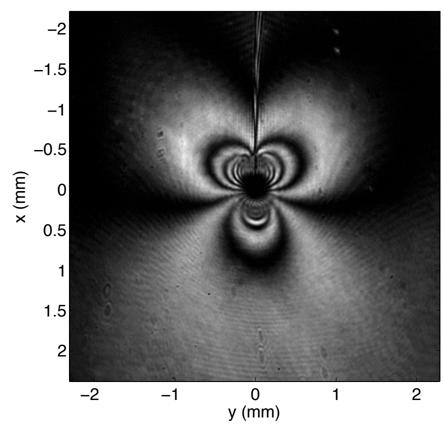

(d) I_4^{circ}

Figure 4.9: Experimental phase-shifted images from vertical shearing CGS using the $\lambda/4$ polarization method for specimen HomC1 for $K_I = 0.514$ MPa$\sqrt{\text{m}}$ and $K_{II} = 4.4$ kPa$\sqrt{\text{m}}$

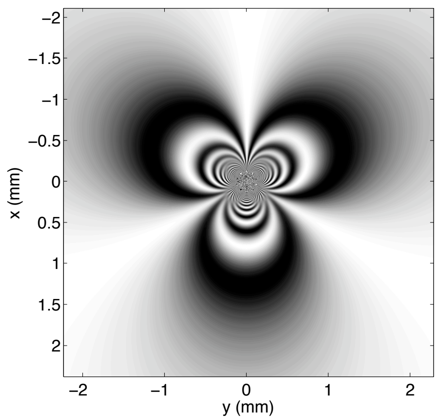

(a) I_1^{circ}

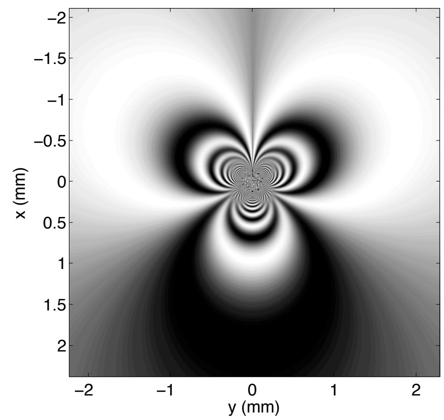

(b) I_2^{circ}

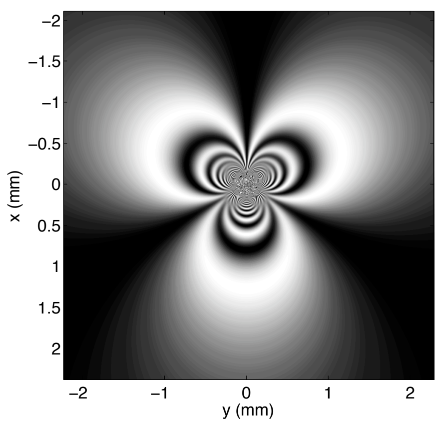

(c) I_3^{circ}

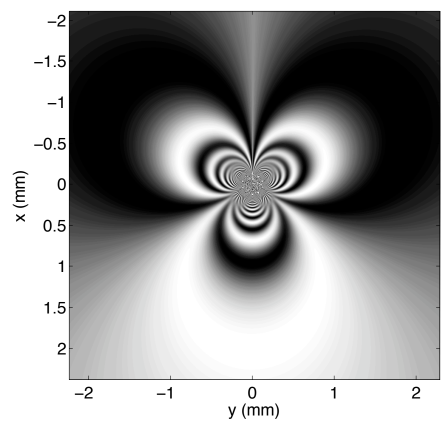

(d) I_4^{circ}

Figure 4.10: Theoretical phase-shifted images from vertical shearing CGS using the $\lambda/4$ polarization method for specimen HomC1 for $K_I = 0.514$ MPa$\sqrt{\text{m}}$ and $K_{II} = 4.4$ kPa$\sqrt{\text{m}}$